Accurate Retinal Vessel Segmentation via Octave Convolution Neural Network

Zhun Fan, *Senior Member, IEEE,* Jiajie Mo, Benzhang Qiu, and Xinjian Chen, *Senior Member, IEEE*

arXiv:1906.12193v5 [eess.IV] 30 Jul 2019

***Abstract*—Retinal vessel segmentation is a crucial step in diagnosing and screening various diseases, including diabetes, ophthalmologic diseases, and cardiovascular diseases. In this paper, we propose an effective and efficient method for vessel segmentation in color fundus images using encoder-decoder based octave convolution network. Compared with other convolution networks utilizing vanilla convolution for feature extraction, the proposed method adopts octave convolution for learning multiple-spatial-frequency features, thus can better capture retinal vasculatures with varying sizes and shapes. It is empirically demonstrated that the feature maps of low-frequency kernels respond mainly to the major vascular tree, whereas the high-frequency feature maps can better capture the fine details of thin vessels. To provide the network the capability of learning how to decode multifrequency features, we extend octave convolution and propose a novel operation named octave transposed convolution. A novel architecture of convolutional neural network is proposed based on the encoder-decoder architecture of UNet, which can generate high resolution vessel segmentation in one single forward feeding. The proposed method is evaluated on four publicly available datasets, including DRIVE, STARE, CHASE_DB1, and HRF. Extensive experimental results demonstrate that the proposed approach achieves better or comparable performance to the state-of-the-art methods with fast processing speed.**

***Index Terms*—Retinal Vessel Segmentation, Multifrequency Feature, Octave Convolution Network.**

I. Introduction

RETINAL vessel segmentation is a crucial prerequisite step of retinal fundus image analysis because retinal vasculatures can aid in accurate localization of other anatomical structures of retina. Retinal vasculature is also extensively used for diagnosis assistance, screening, and treatment planing of ocular diseases such as glaucoma and diabetic retinopathy [1]. The morphological characteristics of retinal vessel such as shape and tortuosity are important indicators for hypertension, cardiovascular and other systemic diseases [2], [3]. These quantitative information obtained from retinal vascular can also be used for early detection of diabetes [4] and progress monitoring of proliferative diabetic retinopathy [5]. Moreover, retinal vasculature can be directly visualized by a non-inversive manner [3], and are routinely adopted by large scale population based studies. Furthermore, retinal vessel segmentation can be utilized for biometric identification because the vessel structure is found to be unique for each individual [6], [7].

In clinical practice, retinal vasculature is often manually annotated by ophthalmologists from fundus images. This manual segmentation is a tedious, laborious, and time-consuming task that requires skill training and expert knowledge. Moreover, it is intuitive and error-prone, which lacks repeatability and reproducibility. To reduce the workload of manual segmentation and improve accuracy, processing speed, and reproducibility of retinal vessel segmentation, a tremendous amount of research efforts have been dedicated in developing fully automated or semiautomated methods for retinal vessel segmentation. However, retinal vessel segmentation is a challenging task due to various complexities of fundus images and retinal structures. Firstly, quality of fundus images can differ due to various imaging artifacts such as blurs, noises, and uneven illuminations [1], [2]. Secondly, various anatomical structures such as optic disc, macula, and fovea are present in fundus images and complicate the segmentation task. Additionally, the possible presence of abnormalities such as exudates, hemorrhages and cotton wool spots pose difficulties to retinal vessel segmentation. Finally, one can argue that the complex nature of retinal vasculatures presents the most significant challenge. The shape, width, local intensity, and branching pattern of retinal vessels vary greatly [2]. If we segment both major and thin vessels with the same technique, it may tend to over segment one or the other [1].

Over the past decades, numerous retinal vessel segmentation methods have been proposed in the literature [1]–[3], [8], [9]. The existing methods can be categorized into unsupervised methods and supervised ones according to whether or not prior information such as vessel groundtruth is utilized as supervision to guide the learning process of a vessel prediction model. Without the need of groundtruth and supervised training, most of the unsupervised methods are rule-based methods, which mainly include morphological approaches [10]–[13], matched filtering methods [14]–[17], multiscale methods [18], [19], and vessel tracking methods [20]–[22].

Supervised methods for retinal vessel segmentation are based on binary pixel classification, i.e., predicting whether a pixel belongs to vessel class or non-vessel class. Traditional machine learning approaches involve two steps: feature

Z. Fan is with the Department of Electrical and Information Engineering, Shantou University, Shantou 515063, China, and also with the Guangdong Provincial Key Laboratory of Digital Signal and Image Processing, College of Engineering, Shantou University, Shantou 515063, China. (e-mail: zfan@stu.edu.cn).

J. Mo is with the Guangdong Provincial Key Laboratory of Digital Signal and Image Processing, College of Engineering, Shantou University, Shantou 515063, China. (e-mail: jiajiemo@outlook.com).

B. Qiu is with the Guangdong Provincial Key Laboratory of Digital Signal and Image Processing, College of Engineering, Shantou University, Shantou 515063, China. (e-mail: 13bzqiu@stu.edu.cn).

X. Chen is with the School of Electrical and Information Engineering, Soochow University, Suzhou 215006, China, and also with the State Key Laboratory of Radiation Medicine and Protection, Soochow University, Suzhou 215123, China. (e-mail: xjchen@suda.edu.cn).

Manuscript revised on July 29th, 2019.

extraction and classification. The first step involves hand crafting features to capture the intrinsic characteristics of a target pixel. Staal et al. [23] propose a ridge based feature extraction method that exploits the elongated structure of vessels. Soares et al. [24] utilize multiscale 2D Gabor wavelet transformations for feature extraction. Various classifiers such as neural networks [25]–[27], support vector machines [15], and random forests [28], [29] are employed in conjunction with hand crafted features extracted from local patches for classifying the central pixel of patches. The aforementioned supervised methods rely on application dependent feature representations designed by domain experts, which usually involve laborious manual feature design procedures based on experiences. Most of these features are extracted at multiple spatial scales to better capture the varying sizes, shapes and scales of vasculatures. However, hand crafted features may not generalize well, especially in cases of pathological retina and complex vasculatures.

Differing from traditional machine learning approaches, modern deep learning techniques learn hierarchical feature representations through multiple levels of abstraction from fundus images and vessel groundtruths automatically. Li et al. [30] propose a cross modality learning framework employing a de-noising auto-encoder for learning initial features for the first layer of neural network. This approach is extended by Fan et al. in [27], where a stacked de-noising auto-encoder is used for greedy layer-wise pre-training of a feedforward neural network. However, these neural networks are fully connected between adjacent layers, which leads to problems such as over-parameterizing and overfitting for the task of vessel segmentation. Furthermore, the quantity of trainable parameters within a fully connected neural networks is related to the size of input images, which leads to high computational cost when processing high resolution images. To address these problems, Convolutional Neural Networks (CNNs) are employed for vessel segmentation in recent researches. Oliveira et al. [31] combine multiscale stationary wavelet transformation and Fully Convolutional Network (FCN) [32] to segment retinal vasculatures within local patches of fundus images. Another popular encoder-decoder based architecture, UNet [33], is introduced by Antiga et al. [34] for vessel segmentation in fundus image patches. Alom et al. [35] propose the R2-UNet model, which incorporates residual blocks [36], recurrent convolutional neural networks [37], and the macro-architecture of UNet. R2-UNet is designed to segment retinal vessels in local patches of fundus images.

However, these patch based paradigms involve cropping patches of fundus images, processing these patches and then merging the results, which are inefficient and may include redundant computation when cropped patches are overlapped. Moreover, patch based approaches do not account for non-local correlations when classifying the center pixels of the patches, which may lead to failures caused by noises or abnormalities [38]. Fu et al. [38], [39] propose an end-to-end approach named DeepVessel, which is based on applying deep supervision [40] on multiscale and multilevel FCN features and adopting conditional random field formulated as a recurrent neural network [41]. A similar deep supervision strategy is adopted by Mo et al. [42] on a deeper FCN model, which achieves better vessel segmentation performance than DeepVessel [38].

In this paper, we propose an effective and efficient method for accurately segmenting both major and thin vessels in fundus images through automatically learning and decoding hierarchical features with multiple-spatial-frequencies. The main contributions of this work are in three folds:

1) Motivated by the observation that vasculature can be decomposed into low spatial frequency components that describe the smoothly changing structures (e.g., the major vessels) and high spatial frequency components that describe the rapidly changing details in spatial dimensions (e.g., the minor details of thin vessels), we adopt octave convolution (OctConv) [43] for building feature encoder blocks, and use them to automatically learn hierarchical multifrequency features at multiple levels of a neural network. Moreover, we empirically demonstrate these low- and high- frequency features can focus on the major vascular tree and thin vessels respectively by visualizing the kernel responses of octave convolution.
2) For decoding these multifrequency features, we propose a novel basic operation called octave transposed convolution (OctTrConv). OctTrConv takes in feature maps with multiple spatial frequencies and restores their spatial details by learning a set of kernels. Decoder blocks are built with OctTrConv and OctConv, and then utilized for decoding multifrequency feature maps.
3) We also propose a novel encoder-decoder based neural network architecture named Octave UNet, which contains two main components. The encoder utilizes multiple aforementioned multifrequency encoder blocks for hierarchical multifrequency feature learning, whereas the decoder contains multiple aforementioned multifrequency decoder blocks for hierarchical feature decoding. Skip connections similar to those in the vanilla UNet [32] are also adopted to feed additional location-information-rich feature maps to the decoder blocks to facilitate recovering spatial details and generating high-resolution probability vessel map. The proposed Octave UNet can be trained in an end-to-end manner and deployed to produce full-sized vessel maps in a single forward feeding, which is much more efficient than the patch based approaches. Furthermore, Octave UNet achieves better or comparable performance to the state-of-the-art methods on four publicly available datasets, without any preprocessing, complex data augmentation, or post-processing procedures.

The remaining sections are organized as following: Section II presents the proposed method. Section III introduces the datasets and the simple data augmentation technique used in this work. In Section IV, we present the training methodology and implementation details, along with comprehensive experimental results. Finally, we conclude this work in Section V.

II. METHOD

A. Multifrequency feature extraction with OctConv

Retinal vessel forms complex tree-like structure with varying sizes, shapes and vessel widths. Unlike the major vascular tree, the thin vessels often have small vessel widths and low background contrast, which is sometimes even difficult for human observers to distinguish.

As illustrated in Fig.1, the low- and high- frequency components of retinal vasculature focus on capturing major vessels and thin vessels, respectively. Motivated by this observation, we adopt octave convolution (OctConv) [43] as multifrequency features extractor.

The computational graph of OctConv is illustrated in Fig.2. Let X^H and X^L denote the input of high- and low- frequency feature maps, respectively. The high- and low- frequency output of OctConv are given by $\hat{Y}^H = f^{H\to H}(X^H) + f^{L\to H}(X^L)$ and $\hat{Y}^L = f^{L\to L}(X^L) + f^{H\to L}(X^H)$, where $f^{H\to H}$ and $f^{L\to L}$ denote the intra-frequency information updates, whereas $f^{H\to L}$ and $f^{L\to H}$ denote the inter-frequency information exchanges.

Specifically, let $W = \{W^{H\to H}, W^{L\to L}, W^{H\to L}, W^{L\to H}\}$ denote the OctConv kernel composed of a set of convolution kernels with different number of channels, $b = \{b^{H\to H}, b^{L\to L}, b^{H\to L}, b^{L\to H}\}$ denotes the biases, k denotes the size of a square kernel, $\sigma(\cdot)$ denotes the non-linear activation function, and $\lfloor\cdot\rfloor$ denotes the floor operation. The high- and low- frequency responses at location (i,j) are given by (1) and (2) respectively.

$$\begin{aligned}\hat{Y}^H_{(i,j)} &= \hat{Y}^{L\to H}_{(i,j)} + \hat{Y}^{H\to H}_{(i,j)} \\ &= f^{L\to H}(X^L) + f^{H\to H}(X^H) \\ &= \sigma\Big(\sum_{m,n} W^{L\to H}_{(m+\frac{k-1}{2},n+\frac{k-1}{2})}{}^T X^L_{(\lfloor\frac{i}{2}\rfloor+m,\lfloor\frac{j}{2}\rfloor+n)} + b^{L\to H}\Big) \\ &\quad + \sigma\Big(\sum_{m,n} W^{H\to H}_{(m+\frac{k-1}{2},n+\frac{k-1}{2})}{}^T X^H_{(i+m,j+n)} + b^{H\to H}\Big) \quad (1)\end{aligned}$$

$$\begin{aligned}\hat{Y}^L_{(i,j)} &= \hat{Y}^{H\to L}_{(i,j)} + \hat{Y}^{L\to L}_{(i,j)} \\ &= f^{H\to L}(X^H) + f^{L\to L}(X^L) \\ &= \sigma\Big(\sum_{m,n} W^{H\to L}_{(m+\frac{k-1}{2},n+\frac{k-1}{2})}{}^T X^H_{(2i+m+\frac{1}{2},2j+n+\frac{1}{2})} + b^{H\to L}\Big) \\ &\quad + \sigma\Big(\sum_{m,n} W^{L\to L}_{(m+\frac{k-1}{2},n+\frac{k-1}{2})}{}^T X^L_{(i+m,j+n)} + b^{L\to L}\Big) \quad (2)\end{aligned}$$

It is worth mentioning that $f^{L\to L}$ and $f^{H\to H}$ are exactly the vanilla convolution operations, whereas $f^{H\to L}$ is equivalent to first downsampling input by average pooling of a scale of two (i.e., approximating $X^H_{(2i+\frac{1}{2},2j+\frac{1}{2})}$ by using average of all four adjacent locations) and then applying vanilla convolution. Likewise, $f^{L\to H}$ is equivalent to upsampling the output of vanilla convolution by a scale of two, where $X^L_{(\lfloor\frac{i}{2}\rfloor,\lfloor\frac{j}{2}\rfloor)}$ is implemented with nearest neighbor interpolation.

Whereas the original goal of OctConv is to reduce the spatial redundancy of convolutional feature maps based on the assumption that these kernel responses can be decomposed into low- and high- spatial frequency components similar to natural images, we empirically show in Fig.5 that by controlling the scale of receptive fields of the convolution kernels, low- and high- frequency feature maps can learn to focus on the major vascular tree and minor details of thin vessels, respectively.

B. Multifrequency feature decoding with OctTrConv

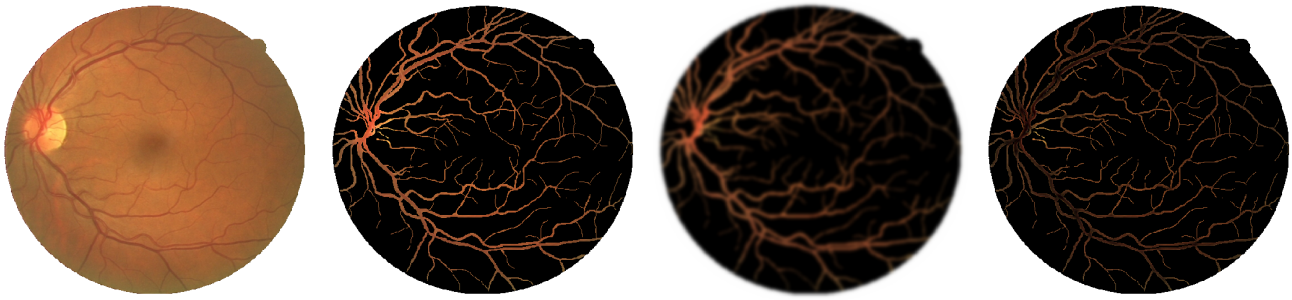
On one hand, during the feature encoding process as shown in Fig.5, while the spatial dimensions of the feature maps reduce gradually, the feature maps lose spatial details step by step. This compression effect forces the kernels to learn more discriminative features with higher levels of abstraction. On the other hand, given only the multifrequency feature extraction is not enough to perform dense pixel classification. A process of decoding feature maps to recover spatial details and generating high resolution vessel map is needed. One naive way of achieving this is to use bilinear interpolation, which lacks the capability of learning the decoding transformation as possessed by vanilla transposed convolution. However, simply using multiple stems of transposed convolution separately lacks information exchange between frequencies, which implies that multiple frequency features should be utilized independently for reconstructing segmentation results, which may not hold true in real world applications.

To address these issues, we extend OctConv and propose a novel operation named octave transposed convolution (OctTrConv), which provides the capability of learning suitable mappings for decoding multifrequency features. As illustrated in Fig.3, OctTrConv takes in feature maps with multiple spatial frequencies and restores their spatial details by learning a set of mappings including intra-frequency information update and inter-frequency information exchange.

The computational graph of OctTrConv is shown in Fig.3. Let X^H and X^L denote the input of high- and low- frequency feature maps, respectively. The high- and low- frequency output of OctTrConv are given by $\hat{Y}^H = g^{H\to H}(X^H) + g^{L\to H}(X^L)$ and $\hat{Y}^L = g^{L\to L}(X^L) + g^{H\to L}(X^H)$, where $g^{H\to H}$ and $g^{L\to L}$ denote the intra-frequency information updates, whereas $g^{H\to L}$ and $g^{L\to H}$ denote the inter-frequency information exchanges.

Similarly, let $W = \{W^{H\to H}, W^{L\to L}, W^{H\to L}, W^{L\to H}\}$ denote the octave kernel composed of a set of trainable kernels, $b = \{b^{H\to H}, b^{L\to L}, b^{H\to L}, b^{L\to H}\}$ denotes the biases, k denotes the size of a square kernel, $\sigma(\cdot)$ denotes the non-linear activation function, and $\lfloor\cdot\rfloor$ denotes the floor operation. The high- and low- frequency responses at location (i,j) are given by (3) and (4) respectively.

$$\begin{aligned}\hat{Y}^H_{(i,j)} &= \hat{Y}^{L\to H}_{(i,j)} + \hat{Y}^{H\to H}_{(i,j)} \\ &= g^{L\to H}(X^L) + g^{H\to H}(X^H) \\ &= \sigma\Big(\sum_{m,n} X^L_{(m+\frac{k-1}{2},n+\frac{k-1}{2})}{}^T W^{L\to H}_{(\lfloor\frac{i}{2}\rfloor+m,\lfloor\frac{j}{2}\rfloor+n)} + b^{L\to H}\Big) \\ &\quad + \sigma\Big(\sum_{m,n} X^H_{(m+\frac{k-1}{2},n+\frac{k-1}{2})}{}^T W^{H\to H}_{(i+m,j+n)} + b^{H\to H}\Big) \quad (3)\end{aligned}$$



(a) Fundus image. (b) Image of vasculature. (c) Low frequency component. (d) High frequency component.

Fig. 1. The image of vasculature can be decomposed into low spatial frequency components that describe the major vascular tree and high spatial frequency components that describe the edges and minor details of thin vessels.

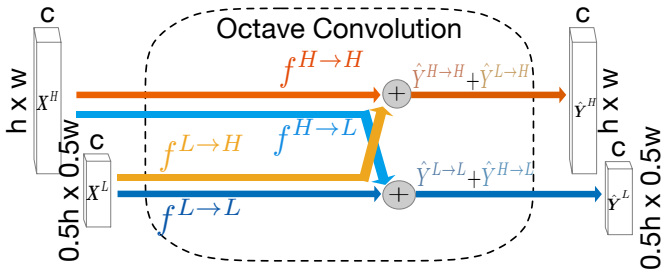


Fig. 2. An abstraction of computation graph for OctConv operation. The OctConv contains inter-frequency information exchange ($f^{L\to H}$ and $f^{H\to L}$) and intra-frequency information update ($f^{L\to L}$ and $f^{H\to H}$). OctConv can be used to produce feature maps with the same resolution as the inputs by controlling the kernel sizes, kernel strides, and padding pattern.

$$
\begin{aligned}
\hat{Y}^L_{(i,j)} &= \hat{Y}^{H\to L}_{(i,j)} + \hat{Y}^{L\to L}_{(i,j)} \\
&= g^{H\to L}(X^H) + g^{L\to L}(X^L) \\
&= \sigma\Big(\sum_{m,n} X^H_{(m+\frac{k-1}{2},n+\frac{k-1}{2})}{}^T W^{H\to L}_{(2i+m+\frac{1}{2},2j+n+\frac{1}{2})} + b^{H\to L}\Big) \\
&\quad + \sigma\Big(\sum_{m,n} X^L_{(m+\frac{k-1}{2},n+\frac{k-1}{2})}{}^T W^{L\to L}_{(i+m,j+n)} + b^{L\to L}\Big) \qquad (4)
\end{aligned}
$$

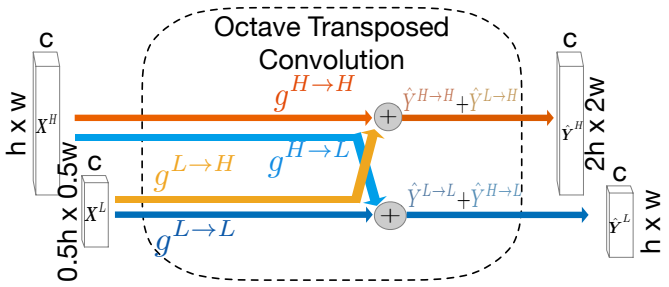


Fig. 3. An abstraction of computation graph for OctTrConv operation. The OctTrConv contains inter-frequency information exchange ($g^{L\to H}$ and $g^{H\to L}$) and intra-frequency information update ($g^{L\to L}$ and $g^{H\to H}$). OctTrConv can upsample feature maps with higher resolution to the inputs by controlling the kernel sizes, kernel strides, and padding pattern.

It is worth notting that $g^{L\to L}$ and $g^{H\to H}$ are exactly the vanilla transposed convolution operations, whereas $g^{H\to L}$ is equivalent to first downsampling input by a scale of two (i.e., approximating $X^H_{(2i+\frac{1}{2},2j+\frac{1}{2})}$ by using average of all four adjacent locations) and then applying vanilla transposed convolution. Likewise, $g^{L\to H}$ is equivalent to upsampling the output of vanilla transposed convolution by a scale of two, where $X^L_{(\lfloor\frac{i}{2}\rfloor,\lfloor\frac{j}{2}\rfloor)}$ is implemented with nearest neighbor interpolation.

C. Octave UNet

In this section, a novel encoder-decoder based neural network architecture named Octave UNet is proposed. After end-to-end training, Octave UNet is capable of extracting and decoding hierarchical multifrequency features for segmenting retinal vasculature in full-sized fundus images. Octave UNet consists of two main processes, i.e., feature encoding and decoding. Building upon the OctConv and OctTrConv operations, we design multifrequency feature encoder blocks and decoder blocks for hierarchical multifrequency feature learning and decoding respectively. By stacking multiple encoder blocks sequentially as in Fig.4, hierarchical multifrequency features can learn to capture both the low frequency components that describe the smoothly changing structures such as the major vessels, and high frequency components that describe the rapidly changing details including the fine details of thin vessels, as shown in Fig.5.

According to the feature encoding sequence shown in Fig.4, the feature maps lose spatial details and location information, while the spatial dimensions of the feature maps reduce gradually. One example of this effect is shown in Fig.5. Only using features of high-abstract-level that lack location information is insufficient for generating precise segmentation results. Inspired by the vanilla UNet [32], skip connections are adopted to concatenate low-level location-information-rich features to the inputs of decoder blocks as shown in Fig.4. According to the proposed Octave UNet architecture shown in Fig.4, stack of decoder blocks in combination with skip connections can facilitate the restoration of location information and spatial details, with one example illustrated in Fig.5.

It is worth mentioning that, the initial OctConv layer of Octave UNet in Fig.4 contains only computation of $\hat{Y}^H = f^{H\to H}(X^H)$ and $\hat{Y}^L = f^{H\to L}(X^H)$, where X^H is the

input of fundus image and the computation involving X^L is discarded. Similarly, the final OctConv layer in Fig.4 contains only computation of $\hat{Y}^H = f^{H\to H}(X^H) + f^{L\to H}(X^L)$, where $\hat{Y}^H$ is the probability vessel map output of Octave UNet and the computation for $\hat{Y}^L$ is discarded. Except for the final OctConv layer that is activated by sigmoid function ($\sigma(x) = \frac{1}{1+e^{-x}}$) for performing binary classification, ReLU activation [44] ($\sigma(x) = \max(x, 0)$) is adopted for all the other layers. Batch normalization [45] is also applied in every OctConv and OctTrConv layers. Octave UNet can be trained in an end-to-end manner on sample pairs of full-size fundus images and vessel groundtruths.

III. Material

A. Datasets

The proposed method is evaluated on four publicly available retinal fundus image datasets: DRIVE [23], STARE [46], CHASE_DB1 [47], and HRF [48]. An overview of these 4 publicly available datasets is provided in Table I.

TABLE I
OVERVIEW OF DATASETS ADOPTED IN THIS PAPER.

Dataset	Year	Description	Resolution
DRIVE	2004	40 in total, 20 for training, 20 for testing.	565×584
STARE	2000	20 in total, 10 are abnormal.	700×605
CHASE_DB1	2011	28 in total.	999×960
HRF	2011	45 in total, 15 each for healthy, diabetic and glaucoma.	3504×2336

B. Data preprocessing and augmentation

No major preprocessing and post-processing steps are needed in this implementation. Only horizontal and vertical random flip are adopted as a simple technique of data augmentation.

IV. Experiments

A. Evaluation metrices

Retinal vessel segmentation is often formulated as a binary dense classification task, i.e., predicting each pixel belonging to positive (vessel) or negative (non-vessel) class within an input image. As shown in Table II, a pixel prediction can fall into one of the four categories, i.e., True Positive (TP), True Negative (TP), False Positive (FP), and False Negative (FN). By plotting these pixels with different color, e.g., TP with Green, FP with Red, TN with Black, and FN with Blue, an analytical vessel map can be generated, as shown in Fig.7.

As listed in Table III, we adopt five commonly used metrices for evaluation: accuracy (ACC), sensitivity (SE), specificity (SP), F1 score (F1), and Area Under Receiver Operating Characteristic curve (AUROC).

For methods that use binary thresholding to obtain the final segmentation results, ACC, SE, SP and F1 are dependent

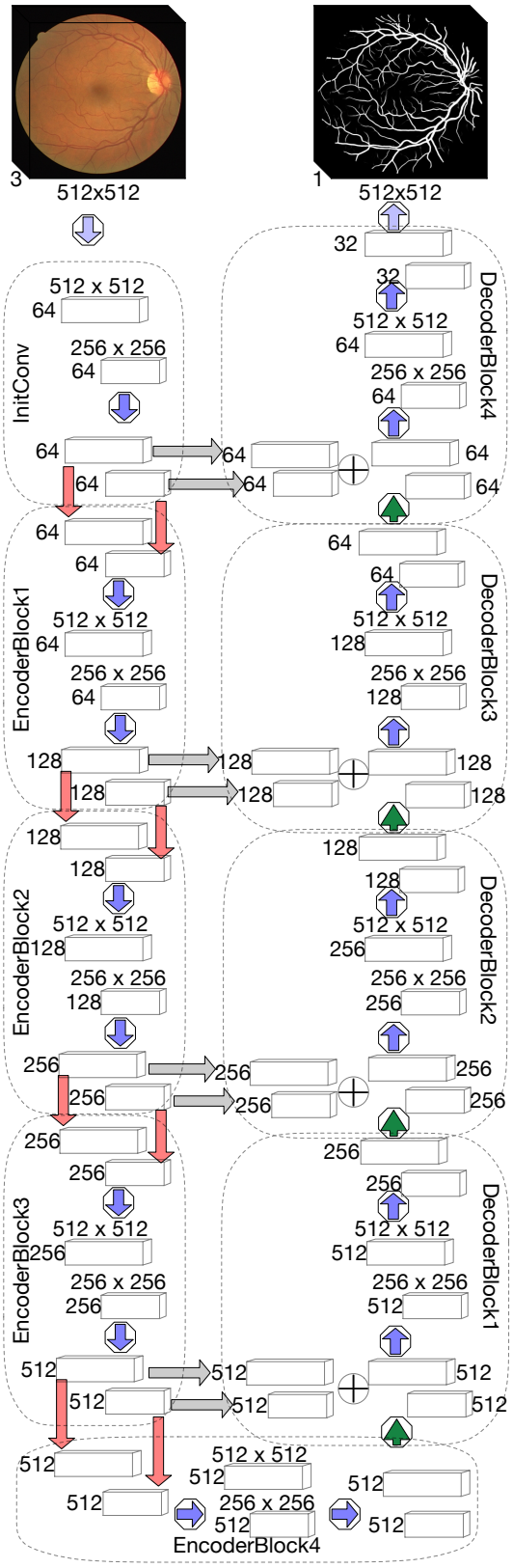
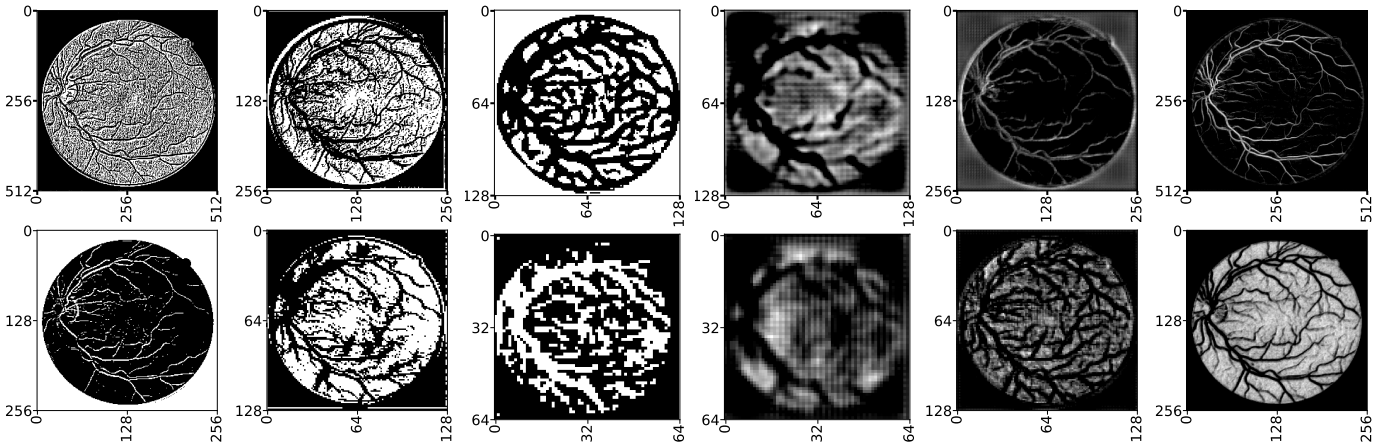


Fig. 4. The detailed architecture of Octave UNet. Feature maps are denoted as cubics with number of channels on the side and spatial dimensions on top. The spatial dimensions of feature maps remained the same within an encoder or decoder block. OctConv and OctTrConv operations are denoted by a blue and green arrow within an octagon, respectively. The red arrows denote max pooling operations that downsample input by a scale of two. The gray arrows denote skip connections that copy and concatenate feature maps. The concatenation operations for skip connections are denoted by a plus sign.



(a) InitConv. (b) Encoder1. (c) Encoder2. (d) Decoder2. (e) Decoder3. (f) Decoder4.

Fig. 5. High (first row) and low (second row) frequency kernel responses of encoders and decoders at different abstract level. The first 3 columns show feature maps from different encoders, while the last 3 columns show the reconstructed vessel map from different decoders.

TABLE II
A BINARY CONFUSION MATRIX FOR VESSEL SEGMENTATION.

Predicted class	Groundtruth class	
	Vessel	Non-vessel
Vessel	True Positive (TP)	False Negative (FN)
Non-vessel	False Positive (FP)	True Negative (TP)

TABLE III
EVALUATION METRICES ADOPTED IN THIS WORK.

Evaluation metric	Description
accuracy (ACC)	ACC = (TP + TN) / (TP + TN + FP + FN)
sensitivity (SE)	SE = TP / (TP + FN)
specificity (SP)	SP = TN / (TN + FP)
F1 score (F1)	F1 = (2 * TP) / (2 * TP + FP + FN)
AUROC	Area Under the ROC curve.

on the binarization method. In this paper, without special mentioning, all threshold-sensitive metrices are calculated with global thresholding by threshold $\tau = 0.5$. On the other hand, calculating the area under ROC curve requires first creating the ROC curve by plotting the sensitivity (or True Positive Rate, TPR) against the false positive rate (FPR, FPR = FP / (TP + FN)) at various threshold values. For a perfect model that can segment retinal vasculatures with zero error, its ACC, SE, SP, F1 and AUROC should all hit the best score: one.

B. Experiment setup

1) Loss function: To alleviate the effect of imbalanced-classes problem, i.e., the vessel pixel to non-vessel pixel ratio is about $1/9$, class weighted binary cross-entropy as shown in (5) is adopted as loss function for training, where the positive class weight $w_{pos} = p_{pos}/p_{neg}$ is calculated as the ratio of the positive pixel count p_{pos} to the negative pixel count p_{neg} of the training set. Equation (5) measures the loss of a batch of m samples, in which y_n and $\hat{y}_n$ denote the groundtruth and model prediction of n-th sample, respectively.

$$L = -\sum_{n=1}^{m} \left(w_{pos} y_n \log\left(\hat{y}_n\right) + \left(1 - y_n\right) \log\left(1 - \hat{y}_n\right) \right) \quad (5)$$

2) Training details: The proposed Octave UNet is trained with Adam optimizer [49] with default hyper-parameters (e.g., $\beta_1 = 0.9$ and $\beta_2 = 0.999$). The initial learning rate is set to $\eta = 0.001$. A shrinking schedule is applied for the current learning rate η_i as $\eta_i = 0.95 * \eta_{i-1}$ after the value of loss function has been saturated for 20 epochs. The training process runs for a total of 500 epochs. All trainable kernels are initialized with He initialization [50], and no pre-trained parameters are used.

3) Training and testing set splitting: Except for the DRIVE dataset which has a conventional splitting of training and testing set, the strategy of leave-one-out validation is adopted for STARE, CHASE_DB1, and HRF datasets. Specifically, all images are tested using a model trained on the other images within the same dataset. This strategy for generating training and testing set is also adopted by recent works in [23], [30], [42], [51]. Only the results on test samples are reported in this paper.

C. Experimental results

Average performance measures with standard deviation of the proposed method are shown in Table IV, which demonstrates that the proposed method outperforms the segmentation produced by the second human observers consistently, with only one exception for SE measure on STARE dataset.

The best and worst performances are also illustrated in Fig.6. The best cases on all datasets contain very few missed thin vessels. On the other hand, the worst cases show that the proposed method are effected by uneven illumination. In both best and worst cases, the proposed method is capable of discriminatively separating non-vascular structures and vasculatures.

As shown in Fig.7, one can argue that the proposed method not only can detect major vascular tree, but also is sensitive to

TABLE IV
AVERAGE PERFORMANCE MEASURES WITH STANDARD DEVIATION FOR DRIVE, STARE, CHASE_DB1, AND HRF. IF TWO SETS OF MANUAL ANNOTATIONS ARE PROVIDED FOR A SAME DATASET, THE PERFORMANCES OF THE SECOND HUMAN OBSERVER IS OBTAINED BY EVALUATING THE SECOND SET OF ANNOTATIONS AGAINST THE FIRST SET OF ANNOTATIONS.

Dataset	Method	ACC	SE	SP	F1	AUROC
DRIVE	the proposed method	**0.9661** $\pm$ 0.0033	**0.7957** $\pm$ 0.0584	**0.9827** $\pm$ **0.0044**	**0.8033** $\pm$ **0.0184**	0.9818 $\pm$ 0.0058
	2nd human observer	0.9637 $\pm$ **0.0032**	0.7760 $\pm$ **0.0583**	0.9819 $\pm$ 0.0054	0.7882 $\pm$ 0.0203	N/A
STARE	the proposed method	**0.9742** $\pm$ **0.0055**	0.8164 $\pm$ **0.0647**	**0.9870** $\pm$ **0.0034**	**0.8250** $\pm$ 0.0377	0.9892 $\pm$ 0.0055
	2nd human observer	0.9522 $\pm$ 0.0120	**0.8948** $\pm$ 0.1062	0.9563 $\pm$ 0.0179	0.7400 $\pm$ **0.0372**	N/A
CHASE_DB1	the proposed method	**0.9763** $\pm$ **0.0029**	**0.8244** $\pm$ **0.0334**	**0.9874** $\pm$ **0.0031**	**0.8263** $\pm$ **0.0232**	0.9891 $\pm$ 0.0031
	2nd human observer	0.9695 $\pm$ 0.0051	0.7679 $\pm$ 0.0760	0.9852 $\pm$ 0.0055	0.7764 $\pm$ 0.0246	N/A
HRF	the proposed method	0.9714 $\pm$ 0.0047	0.8020 $\pm$ 0.0393	0.9852 $\pm$ 0.0042	0.8079 $\pm$ 0.0411	0.9851 $\pm$ 0.0068
	2nd human observer	N/A	N/A	N/A	N/A	N/A

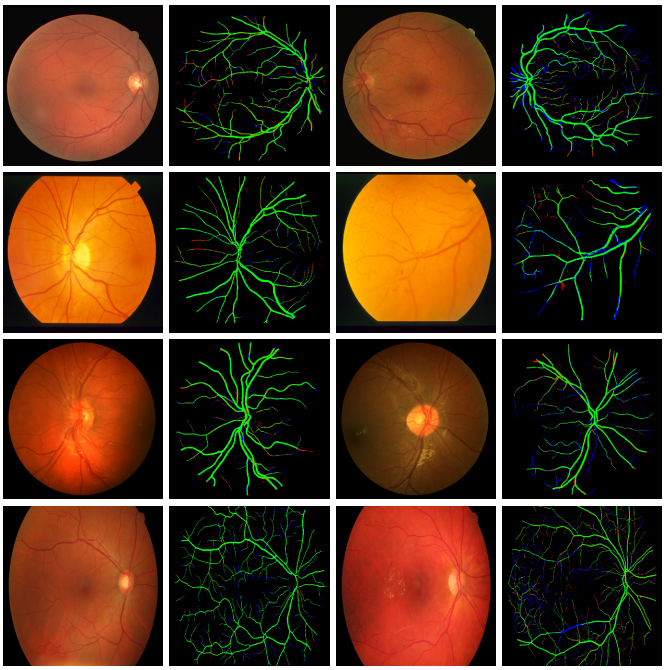


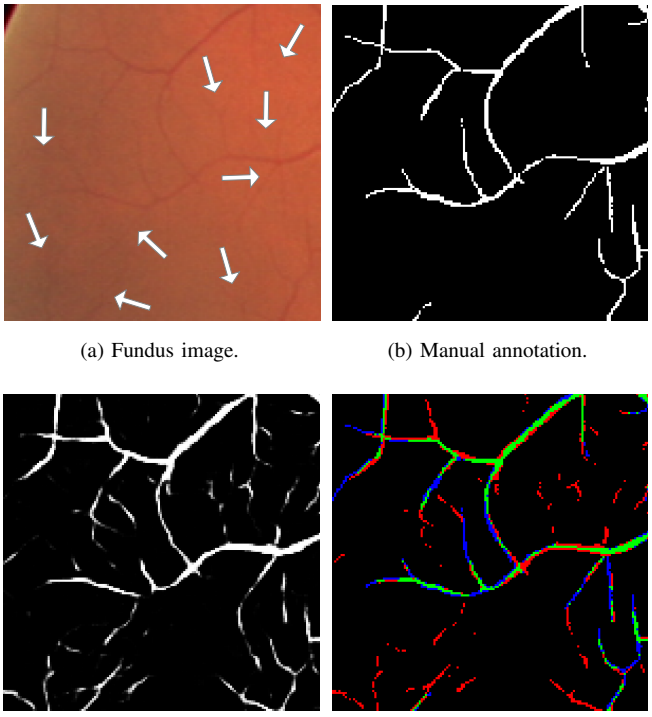
Fig. 6. The best (first 2 columns) and worst (last 2 columns) cases on DRIVE (first row), STARE (second row), CHASE_DB1 (third row) and HRF (last row) datasets.

thin vessels that can be easily overlooked by human observers. The segmentation results of a baseline model of vanilla UNet are also provided in Fig.7. Benefiting from the design of multifrequency feature learning, the proposed Octave UNet can better capture the fine details of thin vessels than the baseline model. Some of the thin vessels are even overlooked by human experts.

Figure.8 illustrates the vessel segmentation performance of the proposed method on complex cases with abnormalities, which demonstrates the robustness of the proposed method against various abnormalities such as exudates, cotton wool spots, hemorrhages, and pathological lesions.

D. Sensitivity analysis of global threshold

The threshold-sensitive metrices: ACC, SE, SP, and F1 are measured at various global threshold values sampled in $\tau_i \in 0.01, \ldots, 0.99$. The resulting sensitivity curves are shown in Fig.9. The sensitivity curves of the proposed method have



(a) Fundus image. (b) Manual annotation.

(c) Predicted probability vessel map of the vanilla UNet. (d) Analytical results of the vanilla UNet.

(e) Predicted probability vessel map of the Octave UNet. (f) Analytical results of the Octave UNet.

Fig. 7. A zoomed in view of segmentation performance of fine details of thin vessels. Many segments detected by vanilla UNet are disconnected, but all vessels detected by Octave UNet are continuous. In addition, some fine details of very small vessels can be detected by the Octave UNet, which are even overlooked by human experts.

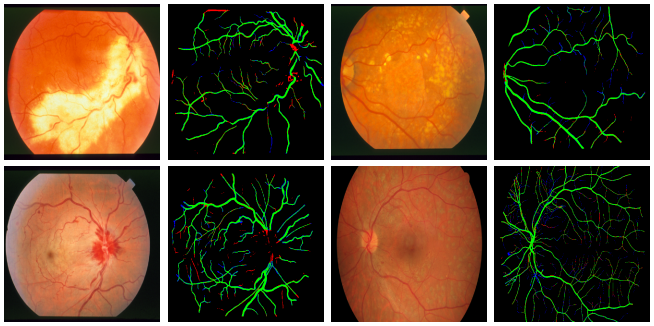
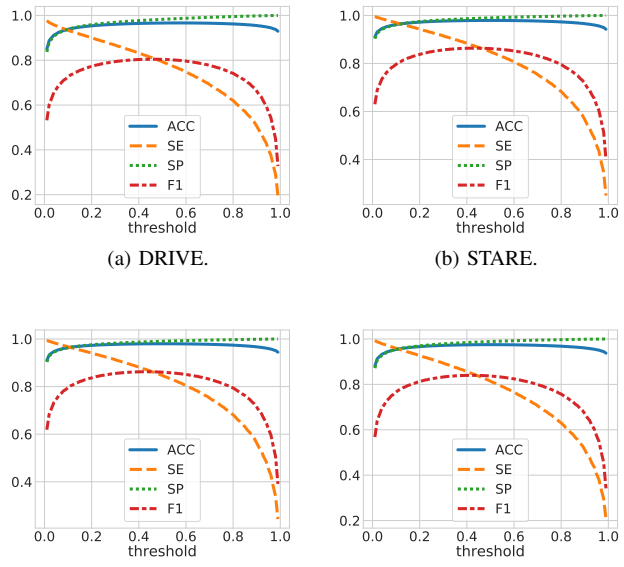


Fig. 8. Original fundus images and analytical vessel segmentation results of cases with exudates, cotton wool spots, hemorrhages, and lesions. The proposed method can segment retinal vasculatures with different types of abnormal regions in fundus images.

almost the same profile on all datasets tested, which demonstrates the robustness of the proposed Octave UNet across different datasets. Furthermore, near the adopted threshold, i.e., $\tau = 0.5$, the sensitivity curves of ACC, SP, and F1 change very slightly, which further demonstrates the robustness of the proposed method against the global threshold. Moreover, by lowering the threshold τ, the proposed method can achieve significant gain on SE, while the other metrices decrease very slightly.



(a) DRIVE. (b) STARE.

(c) CHASE. (d) HRF.

Fig. 9. Sensitivity curves of the proposed method on different datasets.

E. Comparison with other state-of-the-art methods

The performance comparison of the proposed method and the state-of-the-art methods are reported in Table V for DRIVE dataset, Table VI for STARE dataset, Table VII for CHASE_DB1 dataset, and Table VII for HRF dataset.

The proposed method outperforms all other state-of-the-art methods in terms of ACC and SP on all datasets. Specifically, the proposed method achieves the best performance in all five metrices on CHASE_DB1 and HRF datasets. For DRIVE dataset, the proposed method achieves best ACC, SE, SP, and AUROC. Its F1 score is slightly lower than the patch based R2-UNet [52]. For STARE dataset, the proposed Octave UNet obtains metrices of SE, F1, and AUROC comparable to patch based DeepVessel [51] and R2-UNet [52], while achieving best performance on all other metrices. Overall, the proposed method achieves better or comparable performance against the other state-of-the-art methods. It also shows superior performance in comparison with the second human observers in the tested datasets. Experimental results show that it can discern some very fine details of small retinal vessels that are even overlooked by human experts, which implies a great potential of the proposed method.

TABLE V
COMPARISON WITH OTHER STATE-OF-THE-ART METHODS ON DRIVE DATASET.

Methods	Year	ACC	SE	SP	F1	AUROC
Unsupervised Methods						
Zena et al. [10]	2001	0.9377	0.6971	0.9769	N/A	0.8984
Mendonca et al. [11]	2006	0.9452	0.7344	0.9764	N/A	N/A
Al-Diri et al. [20]	2009	0.9258	0.7282	0.9551	N/A	N/A
Miri et al. [12]	2010	0.9458	0.7352	0.9795	N/A	N/A
You et al. [15]	2011	0.9434	0.7410	0.9751	N/A	N/A
Fraz et al. [53]	2012	0.9430	0.7152	0.9768	N/A	N/A
Fathi et al. [26]	2014	N/A	0.7768	0.9759	0.7669	N/A
Roychowdhury et al. [54]	2015	0.9494	0.7395	0.9782	N/A	N/A
Fan et al. [13]	2019	0.9600	0.7360	0.9810	N/A	N/A
Supervised Methods						
Staal et al. [23]	2004	0.9441	0.7194	0.9773	N/A	0.9520
Marin et al. [6]	2011	0.9452	0.7067	0.9801	N/A	0.9588
Fraz et al. [47]	2012	0.9480	0.7460	0.9807	N/A	0.9747
Cheng et al. [55]	2014	0.9472	0.7252	0.9778	N/A	0.9648
Vega et al. [56]	2015	0.9412	0.7444	0.9612	0.6884	N/A
Antiga et al. [34]	2016	0.9548	0.7642	0.9826	0.8115	0.9775
Fan et al. [28]	2016	0.9614	0.7191	0.9849	N/A	N/A
Fan et al. [27]	2016	0.9612	0.7814	0.9788	N/A	N/A
Liskowski et al. [51]	2016	0.9535	0.7811	0.9807	N/A	0.9790
Li et al. [30]	2016	0.9527	0.7569	0.9816	N/A	0.9738
Orlando et al. [57]	2016	N/A	0.7897	0.9684	0.7857	N/A
Mo et al. [42]	2017	0.9521	0.7779	0.9780	N/A	0.9782
Xiao et al. [58]	2018	0.9655	0.7715	N/A	N/A	N/A
Alom et al. [52]	2019	0.9556	0.7792	0.9813	**0.8171**	0.9784
The Proposed Method	2019	**0.9661**	**0.7957**	**0.9827**	0.8033	**0.9818**

F. Computation time

The computation time needed for processing a fundus image from DRIVE dataset using the proposed method is compared with those using other patch based or end-to-end approaches in Table IX. Without the need of cropping and merging patches as in the patch based vanilla UNet [34], the proposed method can generate high-resolution vessel segmentation in a single forward feeding of a full-sized fundus image from DRIVE dataset in $0.4s$.

V. CONCLUSION

An effective and efficient method for retinal vessel segmentation based on multifrequency convolutional network is proposed in this paper. Built upon octave convolution and the proposed octave transposed convolution, Octave UNet can extract hierarchical features with multiple-spatial-frequencies and reconstruct accurate vessel maps. Benefiting from the design of hierarchical multifrequency features, Octave UNet

TABLE VI
COMPARISON WITH OTHER STATE-OF-THE-ART METHODS ON STARE DATASET

Methods	Year	ACC	SE	SP	F1	AUROC
Unsupervised Methods						
Mendonca et al. [11]	2006	0.9440	0.6996	0.9730	N/A	N/A
Al-Diri et al. [20]	2009	N/A	0.7521	0.9681	N/A	N/A
You et al. [15]	2011	0.9497	0.7260	0.9756	N/A	N/A
Fraz et al. [53]	2012	0.9442	0.7311	0.9680	N/A	N/A
Fathi et al. [26]	2013	N/A	0.8061	0.9717	0.7509	N/A
Roychowdhury et al. [54]	2015	0.9560	0.7317	0.9842	N/A	N/A
Fan et al. [13]	2019	0.9570	0.7910	0.9700	N/A	N/A
Supervised Methods						
Staal et al. [23]	2004	0.9516	N/A	N/A	N/A	0.9614
Marin et al. [6]	2011	0.9526	0.6944	0.9819	N/A	0.9769
Fraz et al. [47]	2012	0.9534	0.7548	0.9763	N/A	0.9768
Vega et al. [56]	2015	0.9483	0.7019	0.9671	0.6614	N/A
Fan et al. [28]	2016	0.9588	0.6996	0.9787	N/A	N/A
Fan et al. [27]	2016	0.9654	0.7834	0.9799	N/A	N/A
Liskowski et al. [51]	2016	0.9729	**0.8554**	0.9862	N/A	**0.9928**
Li et al. [30]	2016	0.9628	0.7726	0.9844	N/A	0.9879
Orlando et al. [57]	2016	N/A	0.7680	0.9738	0.7644	N/A
Mo et al. [42]	2017	0.9674	0.8147	0.9844	N/A	0.9885
Xiao et al. [58]	2018	0.9693	0.7469	N/A	N/A	N/A
Alom et al. [52]	2019	0.9712	0.8292	0.9862	**0.8475**	0.9914
The Proposed Method	2019	**0.9741**	0.8164	**0.9870**	0.8250	0.9892

TABLE VII
COMPARISON WITH OTHER STATE-OF-THE-ART METHODS ON CHASE_DB1 DATASET

Methods	Year	ACC	SE	SP	F1	AUROC
Unsupervised Methods						
Fraz et al. [59]	2014	N/A	0.7259	0.9770	0.7488	N/A
Roychowdhury et al. [54]	2015	0.9467	0.7615	0.9575	N/A	N/A
Fan et al. [13]	2019	0.9510	0.6570	0.9730	N/A	N/A
Supervised Methods						
Fraz et al. [47]	2012	0.9469	0.7224	0.9711	N/A	0.9712
Fan et al. [27]	2016	0.9573	0.7656	0.9704	N/A	N/A
Liskowski et al. [51]	2016	0.9628	0.7816	0.9836	N/A	0.9823
Li et al. [30]	2016	0.9527	0.7569	0.9816	N/A	0.9738
Orlando et al. [57]	2016	N/A	0.7277	0.9712	0.7332	N/A
Mo et al. [42]	2017	0.9581	0.7661	0.9793	N/A	0.9812
Alom et al. [52]	2019	0.9634	0.7756	0.9820	0.7928	0.9815
The Proposed Method	2019	**0.9714**	**0.8020**	**0.9853**	**0.8079**	**0.9851**

TABLE VIII
COMPARISON WITH OTHER STATE-OF-THE-ART METHODS ON HRF DATASET

Methods	Year	ACC	SE	SP	F1	AUROC
Unsupervised Methods						
Roychowdhury et al. [54]	2015	0.9467	0.7615	0.9575	N/A	N/A
Supervised Methods						
Kolar et al. [48]	2013	N/A	0.7794	0.9584	0.7158	N/A
Orlando et al. [57]	2016	N/A	0.7874	0.9584	0.7158	N/A
The Proposed Method	2019	**0.9763**	**0.8244**	**0.9874**	**0.8079**	**0.9891**

TABLE IX
COMPARISON OF COMPUTATION TIME OF THE PROPOSED METHOD WITH OTHER APPROACHES ON A DRIVE DATA SAMPLE.

Methods	Year	Main device	Computation time
patch based approaches			
Antiga et al. [34]	2016	NVIDIA GTX Titan Xp	10.5s
End-to-end approaches			
Mo et al. [42]	2017	NVIDIA GTX Titan Xp	**0.4s**
Fan et al. [13]	2019	NVIDIA GTX Titan Xp	6.2s
The Proposed Method	2019	NVIDIA GTX Titan Xp	**0.4s**

can be trained in an end-to-end manner and achieve better or comparable performance compared with the other state-of-the-art methods.

REFERENCES

[1] C. L Srinidhi, P. Aparna, and J. Rajan, "Recent advancements in retinal vessel segmentation," *Journal of Medical Systems*, vol. 41, no. 4, pp. 70–99, Apr 2017.

[2] M. M. Fraz, P. Remagnino, A. Hoppe, B. Uyyanonvara, A. R. Rudnicka, C. G. Owen, and S. A. Barman, "Blood vessel segmentation methodologies in retinal images - a survey," *Computer Methods and Programs in Biomedicine*, vol. 108, no. 1, pp. 407–433, Oct 2012.

[3] P. Vostatek, E. Claridge, H. Uusitalo, M. Hauta-Kasari, P. Fält, and L. Lensu, "Performance comparison of publicly available retinal blood vessel segmentation methods," *Computerized Medical Imaging and Graphics*, vol. 55, pp. 2–12, Jan 2017.

[4] C. Heneghan, J. Flynn, M. O'Keefe, and M. Cahill, "Characterization of changes in blood vessel width and tortuosity in retinopathy of prematurity using image analysis," *Medical Image Analysis*, vol. 6, no. 4, pp. 407–429, Dec 2002.

[5] R. A. Welikala, J. Dehmeshki, A. Hoppe, V. Tah, S. Mann, T. H. Williamson, and S. A. Barman, "Automated detection of proliferative diabetic retinopathy using a modified line operator and dual classification," *Computer Methods and Programs in Biomedicine*, vol. 114, no. 3, pp. 247–261, May 2014.

[6] C. Mariño, M. G. Penedo, M. Penas, M. J. Carreira, and F. Gonzalez, "Personal authentication using digital retinal images," *Pattern Analysis and Applications*, vol. 9, no. 1, pp. 21–33, May 2006.

[7] C. Kose and C. Ikibas, "A personal identification system using retinal vasculature in retinal fundus images," *Expert Systems with Applications*, vol. 38, no. 11, pp. 13 670–13 681, Oct 2011.

[8] T. A. Soomro, A. J. Afifi, L. Zheng, S. Soomro, J. Gao, O. Hellwich, and M. Paul, "Deep learning models for retinal blood vessels segmentation: a review," *IEEE Access*, vol. 7, pp. 71 696–71 717, Jun 2019.

[9] S. Moccia, E. De Momi, S. El Hadji, and L. S. Mattos, "Blood vessel segmentation algorithms review of methods, datasets and evaluation metrics," *Computer Methods and Programs in Biomedicine*, vol. 158, pp. 71–91, May 2018.

[10] F. Zana and J. C. Klein, "Segmentation of vessel-like patterns using mathematical morphology and curvature evaluation," *IEEE Transactions on Image Processing*, vol. 10, no. 7, pp. 1010–1019, Jul 2001.

[11] A. M. Mendonca and A. Campilho, "Segmentation of retinal blood vessels by combining the detection of centerlines and morphological reconstruction," *IEEE Transactions on Medical Imaging*, vol. 25, no. 9, pp. 1200–1213, Sep 2006.

[12] M. S. Miri and A. Mahloojifar, "Retinal image analysis using curvelet transform and multistructure elements morphology by reconstruction," *IEEE Transactions on Biomedical Engineering*, vol. 58, no. 5, pp. 1183–1192, May 2010.

[13] Z. Fan, J. Lu, C. Wei, H. Huang, X. Cai, and X. Chen, "A hierarchical image matting model for blood vessel segmentation in fundus images," *IEEE Transactions on Image Processing*, vol. 28, no. 5, pp. 2367–2377, Dec 2019.

[14] S. Chaudhuri, S. Chatterjee, N. Katz, M. Nelson, and M. Goldbaum, "Detection of blood vessels in retinal images using two-dimensional matched filters," *IEEE Transactions on Medical Imaging*, vol. 8, no. 3, pp. 263–269, Sep 1989.

[15] X. You, Q. Peng, Y. Yuan, Y.-m. Cheung, and J. Lei, "Segmentation of retinal blood vessels using the radial projection and semi-supervised approach," *Pattern Recognition*, vol. 44, no. 10-11, pp. 2314–2324, Oct 2011.

[16] Y. Wang, G. Ji, P. Lin, and E. Trucco, "Retinal vessel segmentation using multiwavelet kernels and multiscale hierarchical decomposition," *Pattern Recognition*, vol. 46, no. 8, pp. 2117–2133, Aug 2013.

[17] J. Zhang, B. Dashtbozorg, E. Bekkers, J. P. W. Pluim, R. Duits, and B. M. ter Haar Romeny, "Robust retinal vessel segmentation via locally adaptive derivative frames in orientation scores," *IEEE Transactions on Medical Imaging*, vol. 35, no. 12, pp. 2631–2644, Dec 2016.

[18] E. Ricci and R. Perfetti, "Retinal blood vessel segmentation using line operators and support vector classification," *IEEE Transactions on Medical Imaging*, vol. 26, no. 10, pp. 1357–1365, Oct 2007.

[19] U. T. Nguyen, A. Bhuiyan, L. A. Park, and K. Ramamohanarao, "An effective retinal blood vessel segmentation method using multi-scale line detection," *Pattern Recognition*, vol. 46, no. 3, pp. 703–715, Mar 2013.

[20] B. Al-Diri, A. Hunter, and D. Steel, "An active contour model for segmenting and measuring retinal vessels," *IEEE Transactions on Medical Imaging*, vol. 28, no. 9, pp. 1488–1497, Sep 2009.

[21] I. Liu and Y. Sun, "Recursive tracking of vascular networks in angiograms based on the detection-deletion scheme," *IEEE Transactions on Medical Imaging*, vol. 12, no. 2, pp. 334–341, Jun 1993.

[22] Y. Yin, M. Adel, and S. Bourennane, "Retinal vessel segmentation using a probabilistic tracking method," *Pattern Recognition*, vol. 45, no. 4, pp. 1235–1244, Apr 2012.

[23] J. Staal, M. D. Abramoff, M. Niemeijer, M. A. Viergever, and B. Van Ginneken, "Ridge-based vessel segmentation in color images of the retina," *IEEE Transactions on Medical Imaging*, vol. 23, no. 4, pp. 501–509, Apr 2004.

[24] J. V. B. Soares, J. J. G. Leandro, R. M. Cesar, H. F. Jelinek, and M. J. Cree, "Retinal vessel segmentation using the 2D Gabor wavelet and supervised classification," *IEEE Transactions on Medical Imaging*, vol. 25, no. 9, pp. 1214–1222, Sep 2006.

[25] D. Marin, A. Aquino, M. E. Gegundez-Arias, J. M. Bravo, D. Marin, A. Aquino, M. E. Gegundez-Arias, and J. M. Bravo, "A new supervised method for blood vessel segmentation in retinal images by using gray-level and moment invariants-based features," *IEEE Transactions on Medical Imaging*, vol. 30, no. 1, pp. 146–158, Jan 2011.

[26] A. Fathi and A. R. Naghsh-Nilchi, "General rotation-invariant local binary patterns operator with application to blood vessel detection in retinal images," *Pattern Analysis and Applications*, vol. 17, no. 1, pp. 69–81, Feb 2014.

[27] Z. Fan and J. Mo, "Automated blood vessel segmentation based on de-noising auto-encoder and neural network," in *Proceedings of the International Conference on Machine Learning and Cybernetics*, vol. 2. IEEE, Jul 2016, pp. 849–856.

[28] Z. Fan, Y. Rong, J. Lu, J. Mo, F. Li, X. Cai, and T. Yang, "Automated blood vessel segmentation in fundus image based on integral channel features and random forests," in *Proceedings of the World Congress on Intelligent Control and Automation*. Institute of Electrical and Electronics Engineers Inc., Sep 2016, pp. 2063–2068.

[29] J. Zhang, Y. Chen, E. Bekkers, M. Wang, B. Dashtbozorg, and B. M. ter Haar Romeny, "Retinal vessel delineation using a brain-inspired wavelet transform and random forest," *Pattern Recognition*, vol. 69, pp. 107–123, Sep 2017.

[30] Q. Li, B. Feng, L. Xie, P. Liang, H. Zhang, and T. Wang, "A cross-modality learning approach for vessel segmentation in retinal images," *IEEE Transactions on Medical Imaging*, vol. 35, no. 1, pp. 109–118, Jan 2016.

[31] A. Oliveira, S. Pereira, and C. A. Silva, "Retinal vessel segmentation based on fully convolutional neural networks," *Expert Systems with Applications*, vol. 112, pp. 229–242, Dec 2018.

[32] J. Long, E. Shelhamer, and T. Darrell, "Fully convolutional networks for semantic segmentation," in *Proceedings of the IEEE Conference on Computer Vision and Pattern Recognition*, May 2015, pp. 3431–3440.

[33] O. Ronneberger, P. Fischer, and T. Brox, "U-net: convolutional networks for biomedical image segmentation," in *International Conference on Medical image computing and computer-assisted intervention*, vol. 9351. Springer, Cham, Nov 2015, pp. 234–241.

[34] L. Antiga and S. Orobix, "Retina blood vessel segmentation with a convolutional neural network," 2016. [Online]. Available: https://github.com/orobix/retina-unet

[35] M. Z. Alom, M. Hasan, C. Yakopcic, T. M. Taha, and V. K. Asari, "Recurrent residual convolutional neural network based on U-Net (R2U-Net) for medical image segmentation," *arXiv preprint arXiv:1802.06955*, May 2018.

[36] K. He, X. Zhang, S. Ren, and J. Sun, "Deep residual learning for image recognition," in *Proceedings of the IEEE Conference on Computer Vision and Pattern Recognition*, Dec 2016, pp. 770–778.

[37] M. Liang and X. Hu, "Recurrent convolutional neural network for object recognition," in *Proceedings of the IEEE Conference on Computer Vision and Pattern Recognition*, Jun 2015, pp. 3367–3375.

[38] H. Fu, Y. Xu, S. Lin, D. W. Kee Wong, and J. Liu, "DeepVessel: retinal vessel segmentation via deep learning and conditional random field," in *International Conference on Medical Image Computing and Computer-Assisted Intervention*, S. Ourselin, L. Joskowicz, M. R. Sabuncu, G. Unal, and W. Wells, Eds. Cham: Springer International Publishing, Oct 2016, pp. 132–139.

[39] H. Fu, Y. Xu, D. W. K. Wong, and J. Liu, "Retinal vessel segmentation via deep learning network and fully-connected conditional random fields," in *Proceedings - International Symposium on Biomedical Imaging*, vol. 2016-June, Apr 2016, pp. 698–701.

[40] C.-Y. Lee, S. Xie, P. Gallagher, Z. Zhang, and Z. Tu, "Deeply-supervised nets," in *Proceedings of the Eighteenth International Conference on Artificial Intelligence and Statistics*, ser. Proceedings of Machine Learning Research, vol. 38. San Diego, California, USA: PRML, May 2015, pp. 562–570.

[41] S. Zheng, S. Jayasumana, B. Romera-Paredes, V. Vineet, Z. Su, D. Du, C. Huang, and P. H. S. Torr, "Conditional random fields as recurrent neural networks," in *Proceedings of the IEEE International Conference on Computer Vision*, Dec 2015, pp. 1529–1537.

[42] J. Mo and L. Zhang, "Multi-level deep supervised networks for retinal vessel segmentation," *International Journal of Computer Assisted Radiology and Surgery*, vol. 12, no. 12, pp. 2181–2193, Dec 2017.

[43] Y. Chen, H. Fang, B. Xu, Z. Yan, Y. Kalantidis, M. Rohrbach, S. Yan, and J. Feng, "Drop an octave: reducing spatial redundancy in convolutional neural networks with octave convolution," *arXiv preprint arXiv:1904.05049*, vol. 1, Apr 2019.

[44] V. Nair and G. E. Hinton, "Rectified linear units improve restricted boltzmann machines," in *Proceedings of the 27th International Conference on Machine Learning*, Jun 2010, pp. 807–814.

[45] S. Ioffe and C. Szegedy, "Batch normalization: accelerating deep network training by reducing internal covariate shift," in *Proceedings of the 32nd International Conference on Machine Learning*, vol. 37, Jul 2015, pp. 448–456.

[46] A. D. Hoover, V. Kouznetsova, and M. Goldbaum, "Locating blood vessels in retinal images by piecewise threshold probing of a matched filter response," *IEEE Transactions on Medical Imaging*, vol. 19, no. 3, pp. 203–210, Mar 2000.

[47] M. M. Fraz, P. Remagnino, A. Hoppe, B. Uyyanonvara, A. R. Rudnicka, C. G. Owen, and S. A. Barman, "An ensemble classification-based approach applied to retinal blood vessel segmentation," *IEEE Transactions on Biomedical Engineering*, vol. 59, no. 9, pp. 2538–2548, Sep 2012.

[48] R. Kolar, T. Kubena, P. Cernosek, A. Budai, J. Hornegger, J. Gazarek, O. Svoboda, J. Jan, E. Angelopoulou, and J. Odstrcilik, "Retinal vessel segmentation by improved matched filtering: evaluation on a new high-resolution fundus image database," *IET Image Processing*, vol. 7, no. 4, pp. 373–383, Jun 2013.

[49] D. P. Kingma and J. Ba, "Adam: a method for stochastic optimization," in *Proceedings of the 3rd International Conference on Learning Representations*, Dec 2015.

[50] K. He, X. Zhang, S. Ren, and J. Sun, "Delving deep into rectifiers: Surpassing human-level performance on imagenet classification," in *Proceedings of the IEEE International Conference on Computer Vision*, Dec 2015, pp. 1026–1034.

[51] P. Liskowski and K. Krawiec, "Segmenting retinal blood vessels with deep neural networks." *IEEE Transactions on Medical Imaging*, vol. 35, no. 11, pp. 2369–2380, Nov 2016.

[52] M. Z. Alom, C. Yakopcic, M. Hasan, T. M. Taha, and V. K. Asari, "Recurrent residual U-Net for medical image segmentation," *Journal of Medical Imaging*, vol. 6, no. 1, pp. 1–16, Jan 2019.

[53] M. M. Fraz, S. A. Barman, P. Remagnino, A. Hoppe, A. Basit, B. Uyyanonvara, A. R. Rudnicka, and C. G. Owen, "An approach to localize the retinal blood vessels using bit planes and centerline detection," *Computer Methods and Programs in Biomedicine*, vol. 108, no. 2, pp. 600–616, Nov 2012.

[54] S. Roychowdhury, D. D. Koozekanani, and K. K. Parhi, "Iterative vessel segmentation of fundus images," *IEEE Transactions on Biomedical Engineering*, vol. 62, no. 7, pp. 1738–1749, Feb 2015.

[55] E. Cheng, L. Du, Y. Wu, Y. J. Zhu, V. Megalooikonomou, and H. Ling, "Discriminative vessel segmentation in retinal images by fusing context-aware hybrid features," *Machine Vision and Applications*, vol. 25, no. 7, pp. 1779–1792, Oct 2014.

[56] R. Vega, G. Sanchez-Ante, L. E. Falcon-Morales, H. Sossa, and E. Guevara, "Retinal vessel extraction using lattice neural networks with dendritic processing," *Computers in Biology and Medicine*, vol. 58, pp. 20–30, Mar 2015.

[57] J. I. Orlando, E. Prokofyeva, and M. B. Blaschko, "A discriminatively trained fully connected conditional random field model for blood vessel segmentation in fundus images," *IEEE Transactions on Biomedical Engineering*, vol. 64, no. 1, pp. 16–27, Jan 2016.

[58] X. Xiao, S. Lian, Z. Luo, and S. Li, "Weighted res-UNet for high-quality retina vessel segmentation," *Proceedings of the 9th International Conference on Information Technology in Medicine and Education*, pp. 327–331, Oct 2018.

[59] M. M. Fraz, A. R. Rudnicka, C. G. Owen, and S. A. Barman, "Delineation of blood vessels in pediatric retinal images using decision trees-based ensemble classification," *International Journal of Computer Assisted Radiology and Surgery*, vol. 9, no. 5, pp. 795–811, Sep 2014.